Controlled p-type substitutional doping in large-area monolayer WSe2 crystals grown by chemical vapor deposition

Journal:	*Nanoscale*
Manuscript ID	NR-ART-08-2018-007070.R1
Article Type:	Paper
Date Submitted by the Author:	29-Oct-2018

Complete List of Authors:	Pandey, Sushil; Indian Institute of Technology, Indore, Electrical Engineering Alsalman, Hussain; University of Minnesota System Azadani, Javad; University of Minnesota System Izquierdo, Nezhueyotl; University of Minnesota College of Science and Engineering Low, Tony; University of Minnesota System Campbell, Stephen A.; University of Minnesota College of Science and Engineering, Electrical and Comp Eng

SCHOLARONE™
Manuscripts

Controlled p-type substitutional doping in large-area monolayer WSe_2 crystals grown by chemical vapor deposition

Sushil Kumar Pandey, Hussain Alsalman, Javad Ghasemi Azadani, Nezhueyotl Izquierdo, Tony Low, and Stephen A. Campbell*
Department of Electrical and Computer Engineering, University of Minnesota, 200 Union Street, Minneapolis, Minnesota 55455, USA
*E-mail: campb001@umn.edu

Abstract

Tungsten diselenide (WSe_2) is a particularly interesting 2D material due to its p-type conductivity. Here we report a systematic single-step process to optimize crystal size by variation of multiple growth parameters resulting in hexagonal single crystals up to 165 μm wide. We then show that these large single crystals can be controllably *in-situ* doped with the acceptor Niobium (Nb). First principles calculations suggest that substitutional Nb doping of W would yield p-doping with no gap trap states. When used as the active layer of a field effect transistor (FET), doped crystals exhibit conventional p-type behavior, rather than the ambipolar behaviour seen in undoped WSe_2 FETs. Nb-doped WSe_2 FETs yield a maximum field effect mobility of 116 $cm^2 V^{-1} s^{-1}$, slightly higher than its undoped counterpart, with an on/off ratio of 10^6. Doping reduces the contact resistance of WSe_2, reaching a minimum value of 0.55 kΩ-μm in WSe_2 FETs. The areal density of holes in Nb-doped WSe_2 is approximately double that of undoped WSe_2, indicating that Nb doping is working as an effective acceptor. Doping concentration can be controlled over several orders of magnitudes, allowing it to be used to control: FET threshold voltage, FET off-state leakage, and contact resistance.

Keywords: 2D Materials, WSe_2, Doping, Density Function Theory, Chemical Vapor Deposition

1. Introduction

Two-dimensional (2D) materials beyond graphene such as transitional metal dichalcogenides (TMDCs),[1-3] black phosphorus (BP),[4,5] and silicene[6] have recently attracted significant attention. 2D materials possess weak interlayer *van der Waals* forces and strong intralayer covalent bonds, which makes them prominent candidates for flexible electronic[7,8] and optoelectronic[9-11] applications. TMDCs are a large family of 2D materials with exceptionally diverse properties straddling semiconductors, superconductors, and metals.[1] The energy band gap of semiconducting TMDCs can be tuned by altering the number of layers, strain, chemical composition, and other properties.[1,11-13] The most heavily studied TMDC, MoS_2,[13-18] has demonstrated n-type field effect transistors (FETs) with a high on/off ratio.[19-21] WSe_2 is particularly important because it is one of the very few TMDCs that is naturally p-type.[22,23] WSe_2 is also well suited for application as photodetectors, light-emitting diodes, and photovoltaic devices due to its high absorption coefficient and efficient photoluminescence (PL).[24-27] WSe_2 is also of interest for thermoelectric devices due to its thermal conductivity, which is among the lowest in dense solids.[28]

In past few years, researchers have developed several techniques to synthesize mono or few-layer WSe_2, including mechanical exfoliation,[22,29,30] liquid exfoliation,[31-33] physical vapor deposition,[34] and chemical vapor deposition (CVD).[35-39] Among these methods, CVD has the

best potential for reproducibly fabricating high-quality large-area monolayer single crystals.[35] Controlled growth of both single crystals and continuous thin films of WSe_2 has been achieved recently.[35,38,39] The former is arguably more important because the lack of grain boundaries produces better electronic and optical properties. Two papers on the temperature optimization of WSe_2 growth (Zhou *et al.*[37] and Liu *et al.*[38]) reported the change in WSe_2 crystal properties with WO_3 (i.e. growth) temperature variation. They were able to synthesize crystals up to 30 μm in width. However, the growth parameter space is more detailed than simply focusing on the growth temperature. Very large monolayer crystals (168 μm) were first demonstrated by Chen, et. al.[39] using a two-step nucleation/growth process involving moving the furnace during the run. Furthermore, conditions to achieve these large crystals often vary by growth system including furnace tube diameter, tube conditioning, heated furnace length, boat geometries, and substrate geometry. These details are not given by Chen, either in the paper or in the supplementary information document. We therefore begin by providing a simpler single-step process to produce 165 mm monolayer crystals including a systematic study to provide researchers with a roadmap, showing how source boat temperatures, total gas pressure, and hydrogen partial pressure can be adjusted to affect crystal size, shape, and number of layers. We conclude this section by comparing our optimal conditions to those of Chen, et. al. to show the significant variation in optimal conditions that can be observed.

A major limitation of WSe_2 as applied to FETs is the tendency of monolayer devices to demonstrate a poorly controlled threshold voltage and either ambipolar or p-type behavior, depending on the contact metals.[22,23] Ambipolar behavior, generally observed with the most frequently used metals (Ti, Au, and Ni),[22,23,38] drastically increases the off-state leakage current in FETs and heterojunction diodes.[40] Finally, the high contact resistance typically observed due to the presence of a large Schottky barrier height degrades the performance of most devices.[41-45] Control of the hole concentration in the WSe_2 through doping is needed to address all of these problems.

While there is an significant amount of literature on doping of thin film TMDCs, e.g. chemical doping of exfoliated TMDCs,[41-46] ion implantation methods,[47,48] and introduction of adspecies using Au,[49] K,[50] PEI,[51] or other organics[52], these approaches have important shortcomings. Controlling the chalcogen composition is challenging and can change the band structure[53] and adspecies that are only held by van der Waals forces have stability issues. Some of these approaches inevitably introduce defect states that severely reduce mobility and minority carrier lifetime. In-situ substitutional doping, a standard practice in conventional 3D semiconductors, is the best option for 2D technology as the bonding of the acceptors in the lattice provides excellent long-term stability without degrading performance.

We therefore investigate substitutional doping of large WSe_2 monolayer crystals. The substitutional doping of MoS_2 is by far the most studied of the TMDCs.[44] Very high concentrations of Cs, Rb, K, Na, and Li as well as Nb have been used to reduce contact resistance, although no attempts at doping control were reported.[54, 55] The dopant was assumed to be substitutional, but no evidence has been presented. There are few papers on substitutional doping of 2D materials other than MoS_2. Gao *et al.*[56] reported substitutional doping of Nb in CVD grown WS_2, while Kang *et al.*[57] demonstrated p-doping of monolayer CVD WSe_2 via Se substitutional doping. However, in these two papers, no electrical transport measurement was performed to determine the electrical performance of the TMDC, such as the contact resistance

and the carrier mobility. Only Fu, *et al.* has demonstrated Ta doping of WSe_2, but this was in small, multi-layer flakes of WSe_2.[58]

In this work an acceptor impurity is added to the optimal growth process to both control threshold voltage and reduce contact resistance. This was done using an *in-situ* Nb source. The separation distance between the Nb_2O_5 boat and the WO_3 boat was varied to control the doping concentration. Accompanying first principles calculations strongly suggest that Nb is a substitutional dopant on W sites, and that such configuration provides an electronic structure free of trap states in the bandgap. Finally, devices made with Nb doped crystals, verifying high FET mobility, low ohmic contact resistance, and the ability to shift the threshold voltage.

2. Experimental Results

WSe_2 monolayer crystals were grown on SiO_2/Si substrates in a CVD tube system. Unless otherwise specified, the temperatures of the WO_3 and Se crucibles were maintained at 800 ^oC and 450 ^oC, respectively. The ratio of H_2/Ar was 1:8 and the tube pressure was 760 torr. The sample was placed on top of the WO_3-containing crucible. Basic growth information is provided in the Methods Section. Additional details are provided in the supporting information (SI).

In agreement with earlier work,[37,38] we found that the crystal size increases with increasing WO_3 temperature. Below 700 ^oC only particles and very few small crystals were observed (Fig. 1a). The number of layers also increases with WO_3 temperature. Multilayer crystals start appearing above 800 ^oC, becoming dominant above 900 ^oC. This can be observed by a color change in optical microscopy and was confirmed by a shift in bandgap as seen by photoluminescence. We chose 800 ^oC as an optimum WO_3 boat temperature for the variation of other parameters.

As reported previously,[38] crystal shape is also influenced by growth temperature. Crystals typically have a triangular shape, solely terminated by either W or Se,[38,60] when grown from 700 to 800 ^oC. At 800 ^oC and above, both regular and irregular shapes appear. The latter can be hexagonal or nearly circular, suggesting a mixed termination. Shape can be affected by the arrival flux and sublimation rates of the adspecies and their mobility on the substrate. All three parameters are affected by growth temperature, which is also the WO_3 source temperature. The parameters can shift the growth between the kinetic-controlled (high temperature) and the thermodynamic-controlled (low temperature) regimes.[61] The growth of crystal edges becomes kinetically-controlled (diffusion) in large crystals, resulting in non-straight edge structures.[68]

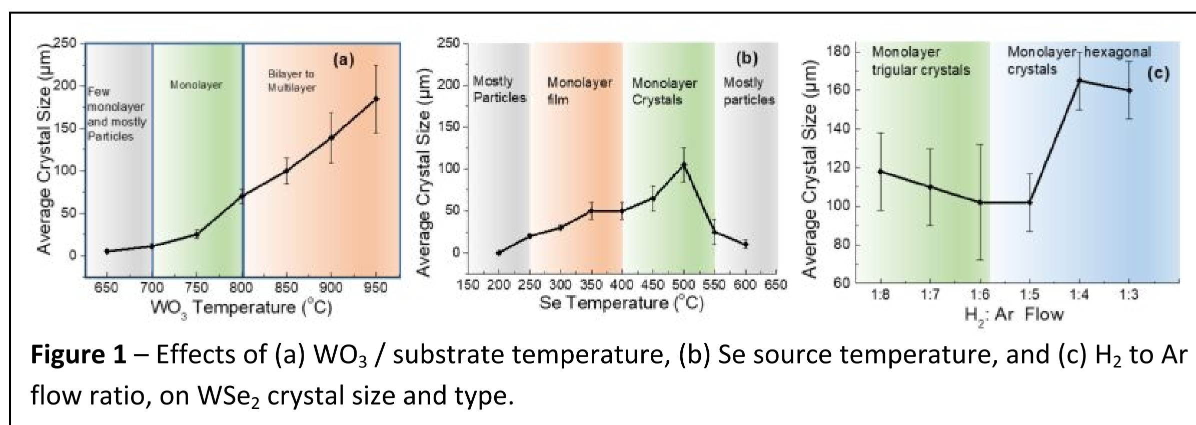

Figure 1 – Effects of (a) WO_3 / substrate temperature, (b) Se source temperature, and (c) H_2 to Ar flow ratio, on WSe_2 crystal size and type.

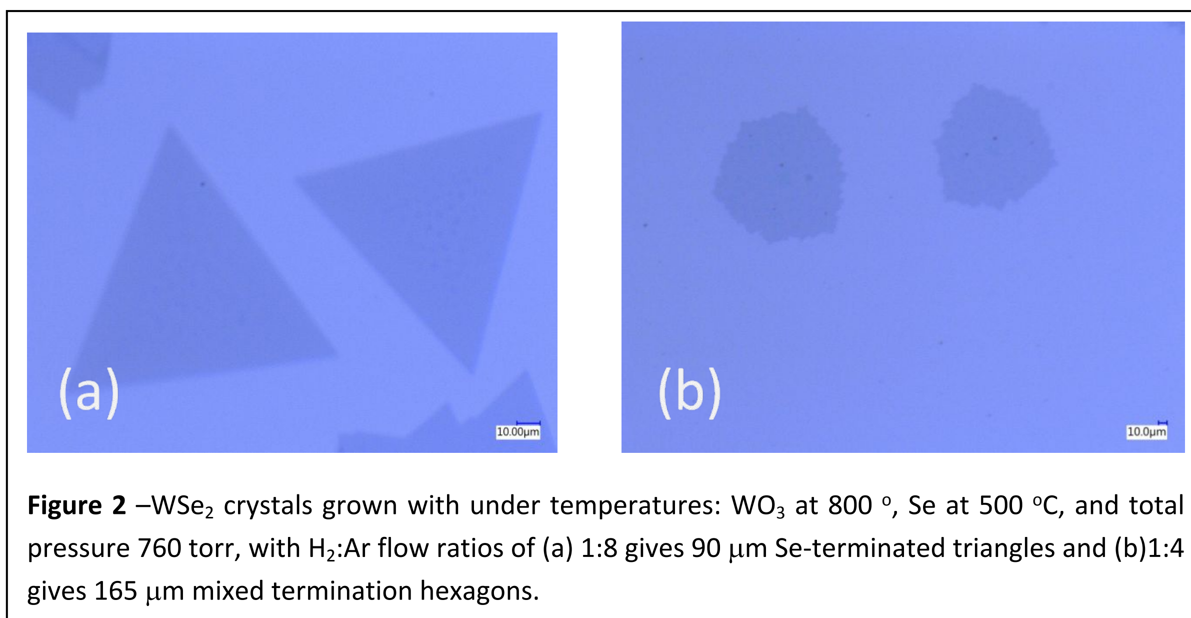

Figure 2 –WSe_2 crystals grown with under temperatures: WO_3 at 800 °, Se at 500 °C, and total pressure 760 torr, with H_2:Ar flow ratios of (a) 1:8 gives 90 μm Se-terminated triangles and (b)1:4 gives 165 μm mixed termination hexagons.

The temperature of the Se boat was then varied. Monolayer WSe_2 films up to 2 mm on a side were observed for growth in the Se temperature range of 250 to 400 °C. The crystals in these films were 20 to 50 μm in width suggesting that the Se flux plays a critical role in the uniform distribution of nucleation points on the substrate, resulting in film growth. If the Se temperature is sufficient to evaporate the Se charge completely, the size of the crystals drops sharply. For Se temperatures above 550 °C only particles are seen on the substrate. Since a Se temperature of 500 °C gave slightly larger crystals, it was used as the baseline condition for the final two steps of the optimization process.

The ratio of the carrier gas (H_2 and Ar) was then varied (Figure 1c). For H_2/Ar ratios from 1:8 to 1:6, most of the sample surface was covered by triangular WSe_2 crystals with very straight edges, indicating a uniform edge structure. Upon further increase of the H_2 partial pressure (increasing the H_2/Ar ratio), the crystal shape changed from triangular to roughly hexagonal. A high partial pressure of H_2 increases the flux of suboxides (WO_{3-x}).[63,64] At low H_2 flows, the crystals are triangular with Se-terminated edges, and the growth rate is set by the rate of WO_{3-x} arrival.[65] It has been suggested that when the ratio of the free energy of Se (γ_{Se}) edges to W (γ_W) edges (γ_{Se}/γ_W) is greater than 2 or less than 0.5, triangular crystals are produced, while hexagonal crystals are produced when $0.5 < \gamma_{Se}/\gamma_W < 2$.[66,67] Under optimal conditions in our reactor, this condition is obtained at a H_2 to Ar flow rate ratio of 1:6. Conversely, hexagonal crystals result for intermediate fluxes of Se and W. The largest hexagonal crystals, with a diagonal width of 165 μm, were observed for a H_2/Ar ratio of 1:4. The image of these crystals in Figure 2b shows a uniform color contrast suggesting uniform thickness. This was confirmed by both AFM and photoluminescence mapping. Since a 1:4 flow rate ratio gave the largest crystals, it was used as the baseline condition for the final step of the optimization process.

	WO_3 Temp (°C)	Se Temp (°C)	H_2/Ar Flow	Pressure (torr)
This Work	800	500	1/4	760
Chen, et. al.	~700	280	1/10	760

Table 1 – A comparison of growth parameters for ~170 μm crystals. Significant differences are seen. These can be attributed to minor but important differences in the deposition systems.

Finally, the growth pressure was varied. As the growth pressure was decreased from 760 torr to 450 torr, the crystal size decreased slightly. The primary effect, however, was that the growth showed poor repeatability, becoming unstable below 450 torr. Even in a single run, the variation in crystal sizes on the sample surface was very large at 450 torr. Thus, a growth pressure of 760 torr was considered optimal. AFM measurements of both WSe_2 triangles and hexagonal crystals were done. Both crystals have thicknesses 0.87 +/- 0.04 nm. The monolayer chalcogen-metal-chalcogen (X-M-X) structure typically have a thickness of 0.9 nm.[38,39,68] The edges of the hexagonal crystal have a jagged morphology, consistent with diffusion-limited growth of Se_2. Table 1 compares the optimal one-step process with the second (growth) step of Chen, et. al.

Once the growth of WSe_2 was optimized, *in-situ* Nb-doping was conducted. Nb_2O_5 powder was kept in a separate boat inside the hot zone of the furnace containing the WO_3 boat. The dopant flux was controlled by changing the separation between the Nb_2O_5 boat and WO_3 boat. Four different separation distances: 0.25”, 1”, 3” and 7” were used to dope the WSe_2 monolayer. Elemental, optical, and electrical properties were measured to estimate the concentration of dopant and carriers.

XPS was used to measure the elemental properties of intrinsic and doped WSe_2 monolayers on SiO_2/Si substrates. We first look at the major constituents: W and Se, in undoped crystals. Figure 3(a) and (b) demonstrate the binding energy profiles for W 4f and Se 3d core levels respectively for intrinsic WSe_2. The binding energy peaks at 32.95 and 35.15 eV are ascribed to the doublet W $4f_{7/2}$ and W $4f_{5/2}$ core levels, respectively. The peaks located at 55.20 and 56.0 eV are attributed to the Se $3d_{5/2}$ and Se $3d_{3/2}$ binding energies. This is consistent with the reported values for the WSe_2.[69] The presence of weak peaks at 35.9 and 38.5 eV correspond to the doublet W $4f_{7/2}$ and W $4f_{5/2}$ for WO_3, respectively. We ascribe this to WO_x suboxide particles occasionally deposited on the surface of WSe_2 and/or near the edge of crystals and exclude these peaks from the analysis. The W to Se ratio calculated from the integrated peak area was 1:2.0 and 1:1.99 for the intrinsic and Nb-doped (3” separation) samples, respectively, well within the measurement uncertainty of the XPS system, indicating good stoichiometry at the optimum growth condition.

XPS was conducted on doped samples grown for boat separations of 0.25”, 3” and 7”. The binding energy peaks at 202.0 and 204.9 eV were detected corresponding to the doublet Nb $3d_{5/2}$ and Nb $3d_{3/2}$ core levels, respectively for the sample prepared using boat separation 0.25” (SI).[70] A Nb concentration of ~1.5% was found for samples grown with a 0.25” separation. XPS results for the 3” and 7” samples showed weak signals that could be correlated to some, but not all, of the expected Nb peaks. As a result, the chemical concentration of Nb in these samples was too low to be reliably extracted.

Raman and PL spectroscopies were performed to reveal the optical quality and layer numbers of intrinsic and Nb-doped WSe_2 hexagonal crystals grown in optimum condition. The PL spectra of intrinsic and Nb-doped (3” separation) WSe_2 hexagonal crystals grown in optimal

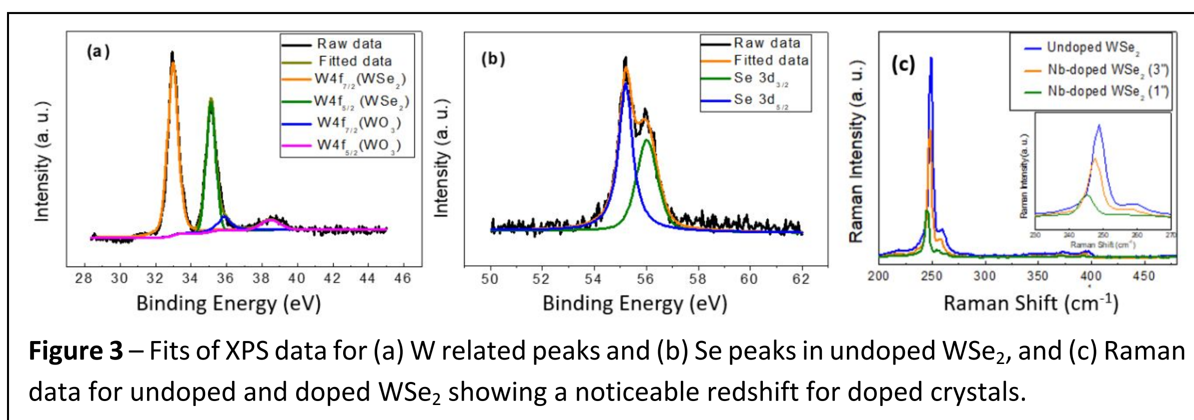

Figure 3 – Fits of XPS data for (a) W related peaks and (b) Se peaks in undoped WSe_2, and (c) Raman data for undoped and doped WSe_2 showing a noticeable redshift for doped crystals.

conditions display strong emission at around 759 nm and 762 nm respectively, a result of the direct band gap transition at the K point. The peak positions and calculated full-width-half-maxima (FWHM) of PL peaks for intrinsic and Nb-doped WSe_2 are 19 nm and 21 nm respectively. Both peak positions and FWHM are in good agreement with previously reported values for exfoliated WSe_2 monolayers.[71,73] Lower peak intensity and higher FWHM are observed for Nb-doped crystals than in intrinsic samples, with PL peak intensity decreasing with increasing doping. This may be due to stress and/or structural defects created by Nb doping. However, PL intensity mapping of the Nb-doped crystal produces a uniform color intensity, suggesting that the Nb doping does not affect the thickness uniformity or create large precipitates. There is a small shoulder present in the PL spectra of intrinsic WSe_2 samples at about 780 nm. This shoulder is more pronounced in Nb-doped samples. The origin is unknown, however the shoulder height appears to scale with the primary peak intensity. A 1" separation produce very broad PL with the highest intensity around 765 nm, suggesting a severely degraded WSe_2 crystallinity. PL spectra of intrinsic and Nb-doped (1" and 3" separation) WSe_2 hexagonal crystal grown under optimum conditions can be found in supporting information.

Raman spectra demonstrate two characteristic peaks at 248.5 and 259 cm^{-1} for intrinsic WSe_2, confirming the E^1_{2g} and A_{1g} modes respectively, as shown in Figure 3(c). The position of these peaks is in good agreement with exfoliated monolayer WSe_2.[71,72] Three high-energy bands at 357.5, 373 and 397 cm^{-1} are also recognized. The Raman peaks at 357.5 and 373 cm^{-1} are attributed to the $2E_{1g}$ and A_{1g}+LA modes.[72] The lack of the $B_{2g}{}^1$ peak at ~307 cm^{-1} again indicates that the hexagonal crystals are monolayer.[38]

The Raman spectra of Nb-doped WSe_2 show E^1_{2g} and A_{1g} peaks at 247.5 and 259.0 cm^{-1} respectively. This agrees with the experimental and theoretical work of Sahin, *et al.*[74] The peak at 250 cm^{-1} shows a red shift whose magnitude increases with doping up to 1.0 cm^{-1} for the 1" separation sample (Fig. 3c). The Raman intensity was found to have a uniform intensity over a large area of the crystal (not shown). Desai, at al. investigated the effects of uniaxial stress on the Raman spectra of WSe_2, finding a blue shift with the application of uniaxial tensile stress.[11] Sahin's work, however, shows that uniaxial and biaxial stress has significantly different effects. The peak observed near 250 cm^{-1} is a degenerate combination of E_{2g} and A_{1g} modes. The combination of the peaks blue shifts under biaxial compressive strain and red shifts slightly under biaxial tensile strain, but the E_{2g} and A_{1g} modes remain degenerate. Uniaxial strain, however, lifts the degeneracy of these two modes.[11] The effect depends of the direction of strain relative to the crystal lattice.[74] First principle calculations described below indicate

that the observed red shift is consistent with biaxial tensile stress created if the doping process involves inserting Nb onto W lattice sites, although we cannot quantify the strain.

The current-voltage (I-V) characteristics of intrinsic and Nb-doped WSe_2 with different boat separations are shown in figure 4(a). The current increases with decreasing boat separation. Samples with a 7" separation showed only a small change compared to the intrinsic WSe_2 monolayer, indicating a doping significantly less than the intrinsic concentration. Since a 1" separation produces optical degradation that we ascribe to stress-related defects, we used 3" separation samples to make transistors. We fabricated back-gated field-effect transistors (FETs) from intrinsic and Nb-doped (1" and 3" separations) WSe_2 crystals grown on 120 nm SiO_2/Si substrates. Transistor measurements were performed under ambient conditions to find the on/off ratios, threshold voltages, and carrier mobilities. The latter two parameters were extracted from the drain to source current (I_{DS}) versus the gate voltage (V_G) transfer characteristics (Figure 4(b)), as described in SI. I_{DS} has been normalized to the channel width. The transfer characteristic exhibits ambipolar and unipolar p-type behavior for intrinsic and Nb-doped devices, respectively. Doping shifts the threshold voltage from -31.5 V for the undoped sample to -36.5 V for the 1" separation sample. This reduction in threshold voltage is due to the higher hole concentration in doped WSe_2 which retards inversion layer formation. From the shift in V_T (5 V) and the estimated oxide capacitance ($3x10^{-8}$ F/cm^2), the difference in the sheet charge density of the WSe_2 is calculated to be $9x10^{11}$ cm^{-2}. Similar (albeit slightly smaller) numbers can be seen in the offset of the extracted TLM sheet carrier density in Figure 4(c). This small difference is likely due to the use of the FET mobility to calculate the ungated TLM carrier density. Given the areal density of W in the lattice ($9.3x10^{14}$ cm^{-2}), this represents an active acceptor concentration of ~0.1%, a value well below the XPS detection limit. We also find that the off-state leakage of the transistor increases with increasing doping as one goes from 3" to 1" separation. This reinforces the suggestion that heavy doping introduces defects, and so increases leakage current.

Both intrinsic and doped devices showed an on/off ratio of 10^6 for V_G swept from −40 to +40 V with a source-drain bias of 0.1 V. However, the off current of the doped device is higher than that of the intrinsic device as shown in Figure 4(b). The maximum field-effect hole mobilities of doped and intrinsic devices are 116 and 43 cm^2 V^{-1} s^{-1}, respectively. The mobilities are comparable to previously reported CVD grown or mechanically exfoliated WSe_2, proving the high crystalline quality of these grown WSe_2 monolayer.[39,62,74] The effect of strain on the band curvature is a possible explanation for this improvement, however the DFT calculations performed (see below) the band curvature slightly increased with doping, indicating a larger effective mass and so a slightly lower mobility. We believe that the observed mobility increase is probably due to increased screening of the coulomb scattering centers as a result of the higher carrier concentration.

The contact resistance was extracted using the transfer length method (TLM). The fabricated TLM structure has an array of two terminal devices with a Ni/Au metal stack on WSe_2 having a channel length varying from 3 to 12 μm and a constant width of 20 μm. All TLM measurements were done in air. It is noteworthy that intrinsic WSe_2 is an ambipolar semiconductor having large Schottky barriers for electrons and holes, producing an extremely large contact resistance (R_C).[75,76] We observed a resistance in the range of 500 GΩ-μm for an

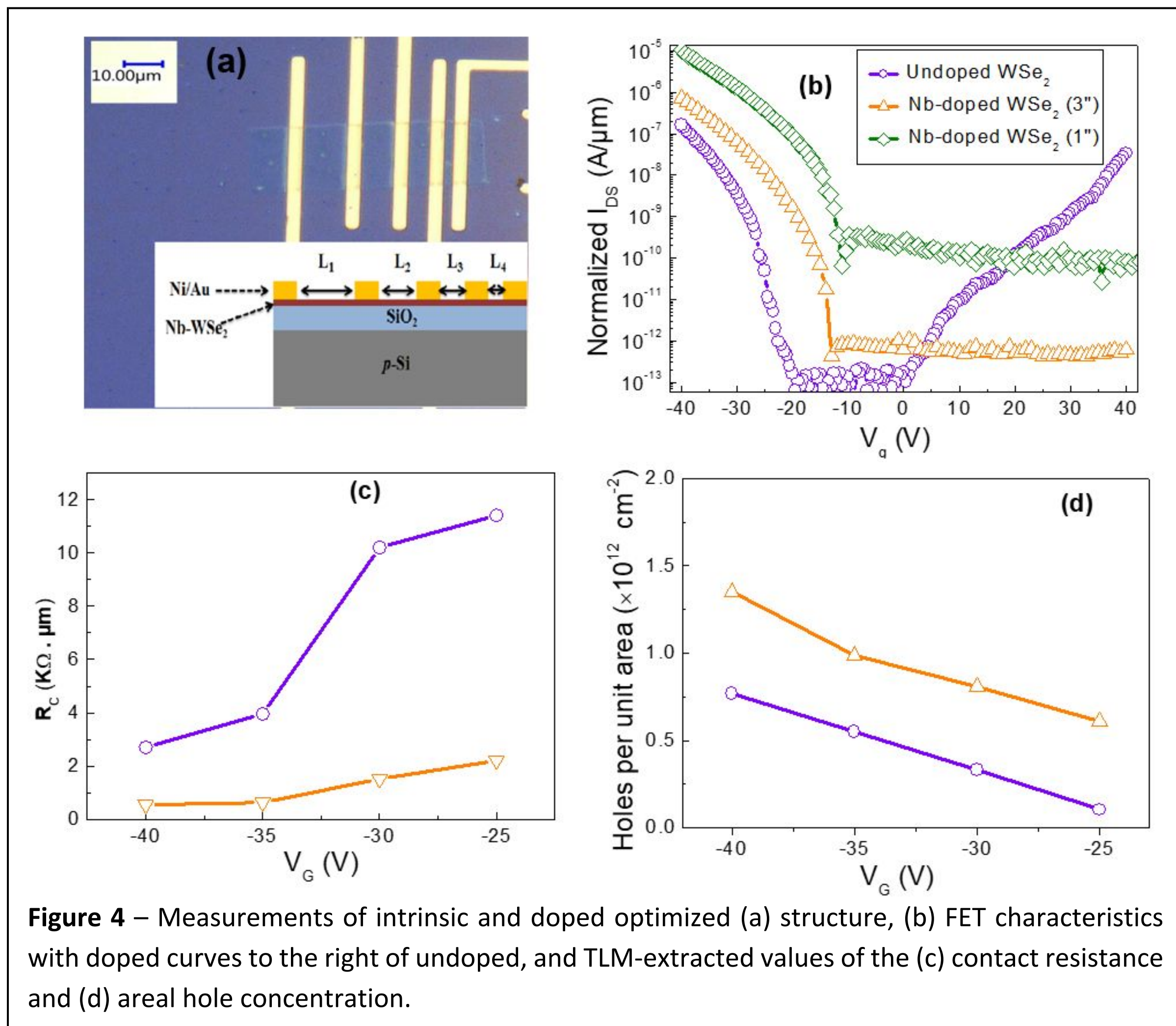

Figure 4 – Measurements of intrinsic and doped optimized (a) structure, (b) FET characteristics with doped curves to the right of undoped, and TLM-extracted values of the (c) contact resistance and (d) areal hole concentration.

intrinsic sample at 0V gate bias. However, contact resistance extraction using a TLM structure is applicable only for relatively low-resistivity contacts. We therefore measured the contact resistance with suitable values of gate bias. Figure 4(c) demonstrates the total resistance and its linear fitting at -40 V gate bias for Nb-doped sample. The output characteristics (I_{DS} versus V_{DS}) of intrinsic and Nb-doped monolayer for 3 μm channel length devices can be found in supporting information. The contact resistance at different gate bias was also measured (Figure 4(c)). We observed that contact resistance of intrinsic as well as doped WSe_2 decreases with the increase of negative gate bias. A minimum value of 0.55 kΩ-μm was achieved at -40 V bias for the doped sample.

The gold contact has a workfunction close to the valence band edge of WSe_2. In intrinsic WSe_2 with no gate bias, the Fermi level is close to the middle of the energy bandgap, ensuring a large Schottky barrier for the injection of holes from the metal contact into the WSe_2. Since thermionic currents exponentially decrease with barrier height, it is unsurprising that the contact resistance is extremely large. Nb-doping of WSe_2, moves the Fermi level closer to the valance band and so dramatically increases the charge injection probability, reducing the contact resistance. Band alignment calculations, discussed below, confirmed the reduction of the Schottky hole barrier. The observed contact resistance at this juncture is lower than that obtained for graphene/WSe_2 contacts which show a resistance of ~2 kΩ-μm.[62] Our Nb-doped

values of contact resistance are comparable to the best results achieved on multilayer TMD devices (~0.2−0.7 kΩ-μm).[58,77,78]

3.0 Corroboration with Density Function Theory

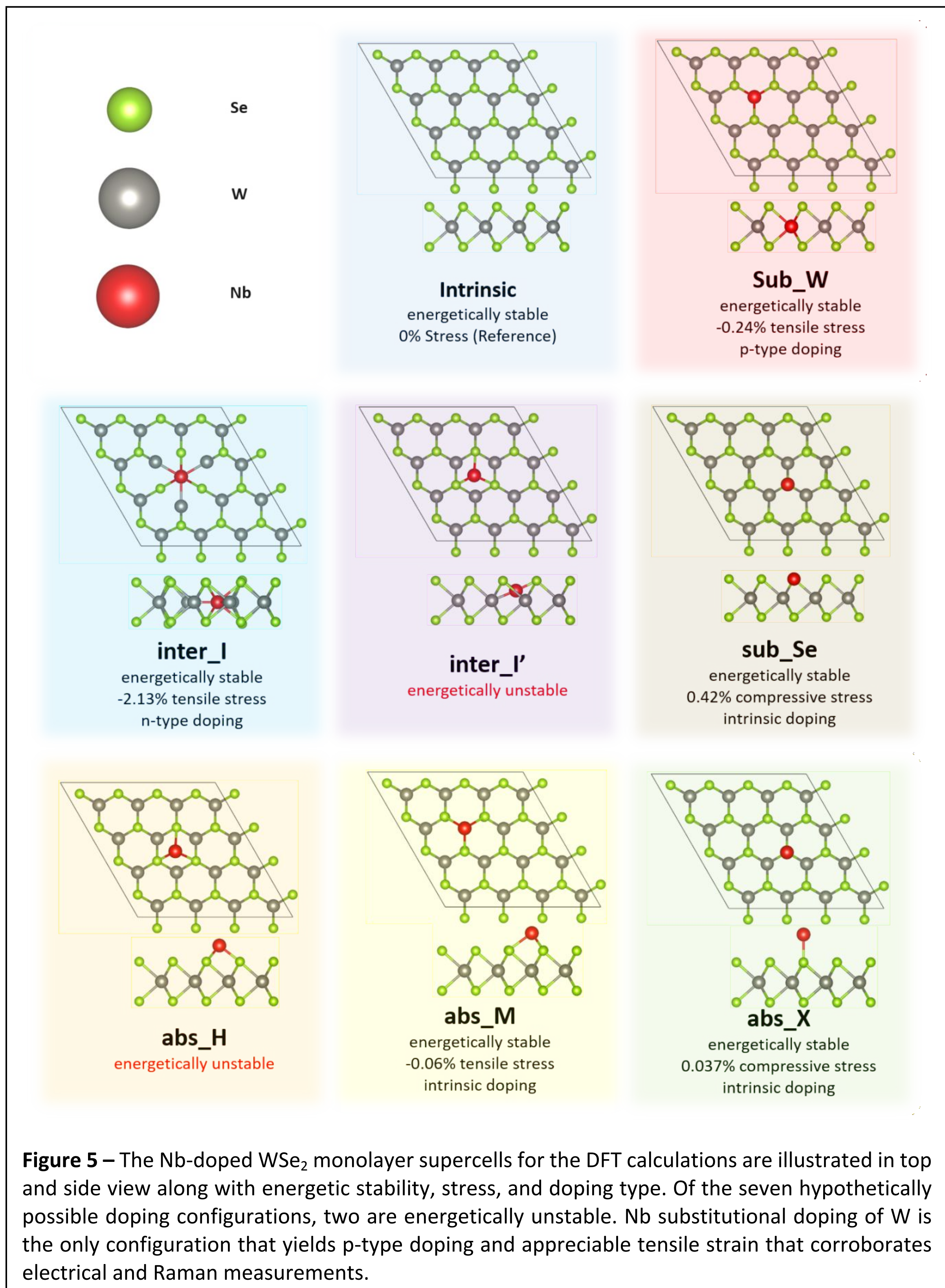

Figure 5 – The Nb-doped WSe_2 monolayer supercells for the DFT calculations are illustrated in top and side view along with energetic stability, stress, and doping type. Of the seven hypothetically possible doping configurations, two are energetically unstable. Nb substitutional doping of W is the only configuration that yields p-type doping and appreciable tensile strain that corroborates electrical and Raman measurements.

Doping of WSe_2 with Nb can lead to modifications in electronic, mechanical and optical properties. For example, the change in electronic bandgap, the induced mechanical strains, and shifts in band alignments and workfunction can be reflected in its photoluminescence, Raman shifts, and contact resistance measurements. We used DFT to connect the experimental observations with predictions from first principles.

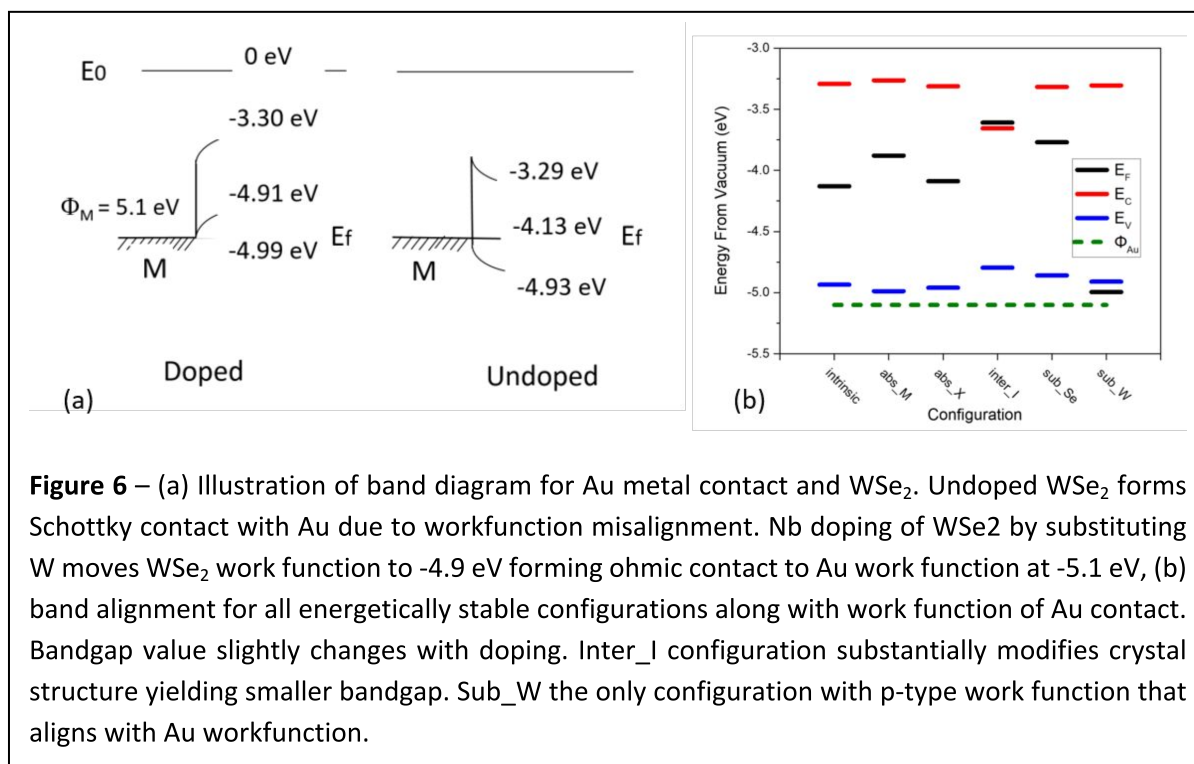

Figure 6 – (a) Illustration of band diagram for Au metal contact and WSe_2. Undoped WSe_2 forms Schottky contact with Au due to workfunction misalignment. Nb doping of WSe2 by substituting W moves WSe_2 work function to -4.9 eV forming ohmic contact to Au work function at -5.1 eV, (b) band alignment for all energetically stable configurations along with work function of Au contact. Bandgap value slightly changes with doping. Inter_I configuration substantially modifies crystal structure yielding smaller bandgap. Sub_W the only configuration with p-type work function that aligns with Au workfunction.

Recent computational investigations[79] suggest that there are seven hypothetically possible configurations of doping WSe_2 with Nb as depicted in Figure 5. Five of them are chemical doping configurations and two are substitutional. The five chemical configurations can be further split into absorption cases and interstitial cases. In absorption, Nb can be absorbed on the surface of WSe_2 on top of a hollow site (abs_H), or on top of a transition metal (abs_M) or on top of a chalcogenide (abs_X). In interstitial, the Nb atom can be trapped interstitially in between the WSe_2 atoms in two possible configurations (inter_I and inter_I'). For the two substitutional doping configurations, Nb could substitute for either the Se atom (sub_Se) or the W atom (sub_W).

In our DFT computations, we have found that two of these seven hypothetical configurations are energetically unstable (abs_H and inter_I') and therefore unlikely scenarios. The second interstitial configuration (inter_I), albeit energetically stable, exhibits very high tensile strain of over 2%, making it rather unlikely. In addition, experimental studies of doping in TMD report absorption and substitutional doping, as elaborated in the introduction section, while none reported interstitial doping. This would leave four possible doping configurations, of which only the W substitutional case (sub_w) yields p-type doping. We discuss the implications of Nb doping via W substitution in the context of the experimental findings.

First, W substitutional doping creates no midgap states in the bandgap. Indeed, our DFT calculations of the electronic bandstructure of the doped WSe_2 confirmed the absence of flat band states within the energy gap. The preservation of carrier mobility after Nb doping is consistent with this prediction. Second, W substitutional doping has a computed p-type work function of 4.9 eV, and its valence band edge is also close to the contact metal (Au) workfunction of 5.1 eV, as depicted in Figure 6. This would explain why the doped WSe_2 can result in a lower resistance ohmic contact. This also explains why the electrical characteristics are that of a p-type semiconductor. Third, the computed stress of the W substitutional doping

indicates an appreciable tensile stress. This is in good agreement with the observed Raman red shift mentioned in the experimental section. In summary, the corroboration between type of doping, strain, and band alignment strongly suggests that the Nb impurity resides primarily on the W sites.

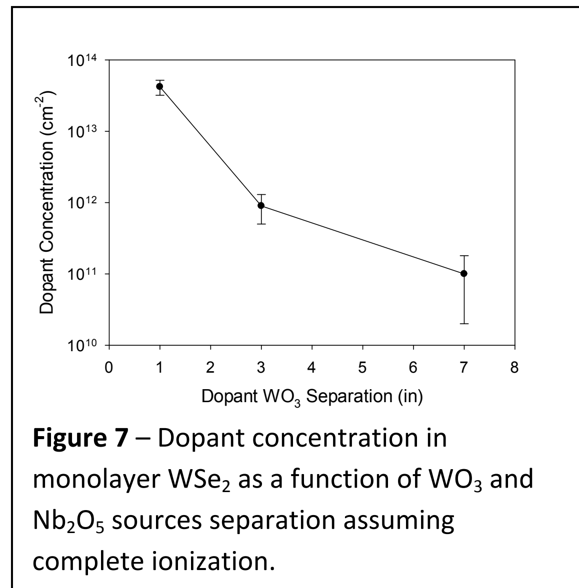

Figure 7 – Dopant concentration in monolayer WSe_2 as a function of WO_3 and Nb_2O_5 sources separation assuming complete ionization.

Since DFT calculations put the Nb acceptor level very close to the valence band maximum, it is reasonable to assume complete ionization at room temperature. Using this approximation, we can compare chemical Nb concentration measured by XPS in the 1" spaced sample, with electrical results measured in the 3" and 7" samples. The results are shown in Figure 7. The doping concentration drops sharply with Nb-source position. Once can use this position to control the doping concentration in WSe_2 (Fig. 7).

4.0 Conclusions

In summary, we report CVD growth of monolayer WSe_2 crystals directly on Si/SiO_2 substrates. We demonstrate that crystal sizes and shapes are controlled by the major growth parameters: WO_3 furnace temperature, Se furnace temperature, total pressure and the H_2/Ar ratio. We observe hexagonal single crystals up to ~165 μm in width. P-type Nb doping of the WSe_2 crystal was performed *in-situ* using optimum growth conditions. FETs fabricated using CVD-grown monolayer intrinsic and Nb-doped WSe_2 show ambipolar and p-type behavior, respectively. Moderate doping produced a change in the sheet carrier concentration of ~$9x10^{11}$ cm^{-2}. The Nb-doped WSe_2 FET shows a maximum mobility of 116 cm^2 V^{-1} s^{-1} with an on/off ratio of 10^6. Additionally, we observed that contact resistance of Nb-doped WSe_2 decreases with both doping and increase of negative gate bias, reaching a minimum value of 0.55 kΩ-μm at -40 V bias for moderately doped crystals. DFT calculations show that Nb is incorporated on W sites. This substitution introduces the tensile stress seen in Raman measurements. However, the substitution does not introduce defect states in the band gap.

5.0 Experimental Section

The substrates were cleaned in a piranha solution (H_2SO_4: H_2O_2 = 4:1) and then heated to 150 ^oC for drying, followed by a hexamethyldisilazane (HMDS) vapor treatment for 5 minutes. Finally, a perylene-3,4,9,10-tetracarboxylic acid tetrapotassium salt (PTAS) solution was applied to the substrate and dried to serve as a growth promoter. A charge of 3 mg of WO_3 powder was placed in a ceramic boat and the substrate was mounted on top of it. This assembly was placed in the center of the heating zone of furnace 1. The furnace used 5" diameter tubes. The Se powder was placed in a separate ceramic boat mounted upstream of the WO_3-containing boat at the center of the furnace 2 heating zone. The temperatures of furnace 1 and 2 were varied from 650 to 950 ^oC and 200 to 600 ^oC, respectively. The detailed temperature profile for optimum growth condition can be found in supplemental materials. Both furnaces were allowed

to naturally cool after growth. For growth of Nb-doped WSe_2, 3 mg of Nb_2O_5 powder in a third boat was kept in the heating zone of furnace 1, upstream of the WO_3-containing boat. The position of the former was varied to change the doping concentration.

Microscopic images and the size of WSe_2 crystals were determined by using a high-resolution Keyence microscope. The thickness and surface image of WSe_2 monolayer crystals were obtained by a Bruker Nanoscope atomic force microscope (AFM) used in contact mode. X-ray photoelectron spectroscopy with Al Kα X-ray source was used to measure the elemental properties of WSe_2. The Raman spectra and map of WSe_2 monolayers were obtained using confocal Raman spectroscopy (WITec Alpha300R) with an Ar laser at 532 nm as the excitation source. The Raman spectroscopy system had a WITec (UHTS 300) detector. To focus the laser beam and to obtain the Raman signal, a 50X objective lens was used. The spot size of the laser beam was 0.5 μm. The same 532 nm laser and a different detector (WITec 2300i) were used to measure and map the photoluminescence spectra.

Device fabrication was done using WSe_2 crystals directly grown on Si/SiO_2 substrates. Optical lithography was used for device formation. A Ni/Au metal (2/60 nm) stack was used as a contact pad for the source and drain regions. Ag paste was used to contact the back of the wafer, which served as the gate electrode. A similar fabrication process was used to fabricate the transfer length method (TLM) structure for measuring the contact resistance. O_2 plasma etching in an Oxford Etcher (180 ICP) was used to etch the WSe_2 in the unwanted areas of the TLM structure. A Precision Semiconductor Parameter Analyser (Hewlett Packard HP Agilent 4156A) was used to measure the electrical characteristics of the fabricated WSe_2 FETs and the TLM structure. Electrical measurements were done at ambient conditions.

Density functional theory (DFT) calculations were carried out using the Vienna ab initio Simulation Package (VASP)[80]. We chose the Perdew-Burke-Ernzerhof (PBE) functional[81] within the generalized gradient approximation (GGA) to treat the exchange-correlation interaction of electrons. We employed projector-augmented wave potentials (PAW).[82] The kinetic energy cut-off for plane-wave basis was chosen as 300 eV for the calculations. A set of $(4 \times 4 \times 1)$ k-point sampling is used for Brillouin zone (BZ) integration in k-space. The convergence criteria of 10-5 eV for total energy and 0.001 eV/Å for force were used for self-consistent calculations and geometry optimization, respectively. A minimum of 17 Å vacuum spacing was added along the direction perpendicular to the 2D plane, in order to avoid the interaction between the adjacent supercells. The crystal structure were constructed using VESTA.[83] Spin Orbital coupling was not included.

Acknowledgements

We acknowledge the support of the National Science Foundation through the National Nano Coordinated Infrastructure (NNCI) program, Award # ECCS-1542202, as the primary funding source for this work. Hussain Alsalman also acknowledges funding from King Abdulaziz City for Science and Technology (KACST).

Conflicts of interest

There are no conflicts to declare.

Supporting Information

Details of the crystal growth procedure, along with details of the materials characterization process (Raman spectroscopy, optical microscopy, photoluminescence, X-ray photoemission spectroscopy, and atomic force microscopy), along with a description of the process for fabricating and measuring back-gated WSe_2 FETs and transmission line structures can be found in the experimental methods section. Micrographs of the many growth results, showing size, shape, and other experimental results including AFM, Raman, and photoluminescence data can also be found in the supporting information (SI) provided with this paper.

References

1. Wang, Q. H.; Kalantar-Zadeh, K.; Kis, A.; Coleman, J. N.; Strano, M. S. Electronics and Optoelectronics of Two Dimensional Transition Metal Dichalcogenides. *Nat. Nanotechnol.* **2012**, 7, 699–712.

2. Wu, W.; Wang, L.; Li, Y.; Zhang, F.; Lin, L.; Niu, S.; Chenet, D. Zhang, X.; Hao, Y.; Heinz, T. F.; *et al.* Piezoelectricity of Single-Atomic-Layer MoS2 for Energy Conversion and Piezotronics. *Nature* **2014**, 514, 470–474.

3. Radisavljevic, B.; Radenovic, A.; Brivio, J.; Giacometti, V.; Kis, A. Single-Layer MoS2 Transistors. *Nat. Nanotechnol.* **2011**, 6, 147–150.

4. Pandey, S.K.; Izquierdo, N; Liptak, R; and Campbell, S. A. Use of a Passivation Layer to Improve Thermal Stability And Quality of a Phosphorene/AZO Heterojunction Diode. *RSC Adv.* **2017**, 7, 46201.

5. Xia, F. N.; Wang, H.; Jia, Y. C. Rediscovering Black Phosphorus as an Anisotropic Layered Material for Optoelectronics and Electronics. *Nat. Commun.* **2014**, 5, 4458.

6. Tao, L.; Cinquanta, E.; Chiappe, D.; Grazianetti, C.; Fanciulli, M.; Dubey, M.; Molle, A.; Akinwande, D. Silicene Field-Effect Transistors Operating at Room Temperature. *Nat. Nanotechnol.* **2015**, 10, 227–231.

7. Chang, H. Y.; Yang, S. X.; Lee, J. H.; Tao, L.; Hwang, W. S.; Jena, D.; Lu, N. S.; Akinwande, D. High-Performance, Highly Bendable MoS2 Transistors with High-K Dielectrics for Flexible Low-Power Systems. *ACS Nano* **2013**, 7, 5446–5452.

8. Akinwande, D.; Petrone, N.; Hone, J. Two-Dimensional Flexible Nanoelectronics. *Nat. Commun.* **2014**, 5, 5678.

9. Pospischil, A.; Furchi, M. M.; Mueller, T. Solar-Energy Conversion and Light Emission in an Atomic Monolayer P-N Diode. *Nat. Nanotechnol.* **2014**, 9, 257–261.

10. Ross, J. S.; Klement, P.; Jones, A. M.; Ghimire, N. J.; Yan, J.; Mandrus, D. G.; Taniguchi, T.; Watanabe, K.; Kitamura, K.; Yao, W.; *et al.* Electrically Tunable Excitonic Light-Emitting Diodes Based on Monolayer WSe2 P-N Junctions. *Nat. Nanotechnol.* **2014**, 9, 268–272.

11. Desai, S. B.; Seol, G.; Kang, J. S.; Fang, H.; Battaglia, C.; Kapadia, R.; Ager, J. W.; Guo, J.; Javey, A. Strain-Induced Indirect to Direct Bandgap Transition in Multilayer WSe2. *Nano Lett.* **2014**, 14, 4592–4597.

12. Fiori, G.; Bonaccorso, F.; Iannaccone, G.; Palacios, T.; Neumaier, D.; Seabaugh, A.; Banerjee, S. K.; Colombo, L. Electronics Based on Two-Dimensional Materials. *Nat. Nanotechnol.* **2014**, 9, 768–779.

13. Duan, X.; Wang, C.; Shaw, J. C.; Cheng, R.; Chen, Y.; Li, H.; Wu, X.; Tang, Y.; Zhang, Q.; Pan, A.; *et al.* Lateral Epitaxial Growth of Two-Dimensional Layered Semiconductor Heterojunctions. *Nat. Nanotechnol.* **2014**, 9, 1024–1030.

14. Lee, Y. H.; Yu, L. L.; Wang, H.; Fang, W. J.; Ling, X.; Shi, Y. M.; Lin, C. T.; Huang, J. K.; Chang, M. T.; Chang, C. S.; *et al.* Synthesis and Transfer of Single-Layer Transition Metal Disulfides on Diverse Surfaces. *Nano Lett.* **2013**, 13, 1852–1857.

15. Ling, X.; Lee, Y. H.; Lin, Y. X.; Fang, W. J.; Yu, L. L.; Dresselhaus, M.; Kong, J. Role of the Seeding Promoter in MoS2 Growth by Chemical Vapor Deposition. *Nano Lett.* **2014**, 14, 464–472.

16. Zhang, X. Q.; Lin, C. H.; Tseng, Y. W.; Huang, K. H.; Lee, Y. H. Synthesis of Lateral Heterostructures of Semiconducting Atomic Layers. *Nano Lett.* **2015**, 15, 410–415.

17. Balendhran, S.; Ou, J. Z.; Bhaskaran, M.; Sriram, S.; Ippolito, S.; Vasic, Z.; Kats, E.; Bhargava, S.; Zhuiykovd, S.; Kalantar-zadeh, K. Atomically Thin Layers of MoS2 via a Two Step Thermal Evaporation-Exfoliation Method. *Nanoscale* **2012**, 4, 461–466.

18. Ji, Q. Q.; Zhang, Y. F.; Gao, T.; Zhang, Y.; Ma, D. L.; Liu, M. X.; Chen, Y. B.; Qiao, X. F.; Tan, P. H.; Kan, M.; *et al.* Epitaxial Monolayer MoS2 on Mica with Novel Photoluminescence. *Nano Lett.* **2013**, 13, 3870–3877.

19. Late, D. J.; Liu, B.; Matte, H. S. S. R.; Dravid, V. P.; Rao, C. N. R. Hysteresis in Single-Layer MoS2 Field Effect Transistors. *ACS Nano* **2012**, 6, 5635–5641.

20. Liu, H.; Neal, A. T.; Ye, P. D. D. Channel Length Scaling of MoS2 MOSFETs. *ACS Nano* **2012**, 6, 8563–8569.

21. Jariwala, D.; Sangwan, V. K.; Wu, C. C.; Prabhumirashi, P. L.; Geier, M. L.; Marks, T. J.; Lauhon, L. J.; Hersam, M. C. Gate Tunable Carbon Nanotube-MoS2 Heterojunction P-N Diode. *Proc. Natl. Acad. Sci. U.S.A.* **2013**, 110, 18076–18080.

22. Fang, H.; Chuang, S.; Chang, T. C.; Takei, K.; Takahashi, T.; Javey, A. High-Performance Single Layered WSe2 p-FETs with Chemically Doped Contacts. *Nano Lett.* **2012**, 12, 3788–3792.

23. Podzorov, V.; Gershenson, M. E.; Kloc, Ch.; Zeis, R.; Bucher, E. High-Mobility Field-Effect Transistors Based on Transition Metal Dichalcogenides. *Appl. Phys. Lett.* **2004**, 84, 3301–3303.

24. Clark, G.; Wu, S.; Rivera, P.; Finney, J.; Nguyen, P.; Cobden, D. H.; Xu, X. Vapor-Transport Growth of High Optical Quality WSe2 Monolayers. *APL Mater.* **2014**, 2, 101101.

25. Ross, J. S.; Klement, P.; Jones, A. M.; Ghimire, N. J.; Yan, J. Q.; Mandrus, D. G.; Taniguchi, T.; Watanabe, K.; Kitamura, K.; Yao, W.; *et al.* Electrically Tunable Excitonic Light-Emitting Diodes Based on Monolayer WSe2 P-N Junctions. *Nat. Nanotechnol.* **2014**, 9, 268–272.

26. Baugher, B. W. H.; Churchill, H. O. H.; Yang, Y. F.; Jarillo, Herrero, P. Optoelectronic Devices Based on Electrically Tunable P-N Diodes in a Monolayer Dichalcogenide. *Nat. Nanotechnol.* **2014**, 9, 262–267.

27. Pospischil, A.; Furchi, M. M.; Mueller, T. Solar-Energy Conversion and Light Emission in an Atomic Monolayer P-N Diode. *Nat. Nanotechnol.* **2014**, 9, 257–261.

28. Chiritescu, C.; Cahill, D. G.; Nguyen, N.; Johnson, D.; Bodapati, A.; Keblinski, P.; Zschack, P. Ultralow Thermal Conductivity in Disordered, Layered WSe2 Crystals. *Science* **2007**, 315, 351–353.

29. Li, H.; Lu, G.; Wang, Y.; Yin, Z.; Cong, C.; He, Q.; Wang, L.; Ding, F.; Yu, T.; Zhang, H. Mechanical Exfoliation and Characterization of Single- and Few-Layer Nanosheets of WSe2, TaS2, and TaSe2. *Small* **2013**, 9, 1974–1981.

30. Novoselov, K. S.; Jiang, D.; Schedin, F.;Booth, T. J.; Khotkevich, V. V.; Morozov, S. V.; Geim, A. K. Two-Dimensional Atomic Crystals. *Proc. Natl. Acad. Sci. U. S. A.* **2005**, 102, 10451–10453.

31. Chhowalla, M.; Shin, H. S.; Eda, G.; Li, L. J.; Loh, K. P.; Zhang, H. The Chemistry of Two-Dimensional Layered Transition Metal Dichalcogenide Nanosheets. *Nat. Chem.* **2013**, 5, 263–275.

32. Green, A. A.; Hersam, M. C. Solution Phase Production of Graphene with Controlled Thickness Via Density Differentiation. *Nano Lett.* **2009**, 9, 4031–4036.

33. Coleman, J. N.; Lotya, M.; O'Neill, A.; Bergin, S. D.; King, P. J.; Khan, U.; Young, K.; Gaucher, A.; De, S.; Smith, R. J.; *et al.* Two-Dimensional Nanosheets Produced by Liquid Exfoliation of Layered Materials. *Science* **2011**, 331, 568–571.

34. Clark, G.; Wu, S. F.; Rivera, P.; Finney, J.; Nguyen, P.; Cobden, D. H.; Xu, X. D. Vapor-Transport Growth of High Optical Quality WSe2 Monolayers. *APL Mater.* **2014**, 2.101101

35. Huang, J. K.; Pu, J.; Hsu, C. L.; Chiu, M. H.; Juang, Z. Y.; Chang, Y. H.; Chang, W. H.; Iwasa, Y.; Takenobu, T.; Li, L. J. Large Area Synthesis of Highly Crystalline WSe2 Mono Layers and Device Applications. *ACS Nano* **2014**, 8, 923–930.

36. Chen, L.; Liu, B. L.; Abbas, A. N.; Ma, Y. Q.; Fang, X.; Liu, Y. H.; Zhou, C. W. Screw-Dislocation-Driven Growth of Two Dimensional few layer and Pyramid-like WSe2 by Sulfur Assisted Chemical Vapor Deposition. *ACS Nano* **2014**, 8, 11543–11551.

37. Zhou, H.; Wang, C.; Shaw, J. C.; Cheng, R.; Chen, Y.; Huang, X.; Liu, Y.; Weiss, N. O.; Lin, Z.; Huang, Y.; *et al.* Large Area Growth and Electrical Properties of p-type WSe2 Atomic Layers. *Nano Lett.* **2015**, 15, 709–713.

38. Bilu Liu, Mohammad Fathi, Liang Chen, Ahmad Abbas, Yuqiang Ma, and Chongwu Zhou Chemical Vapor Deposition Growth of Monolayer WSe2 with Tunable Device Characteristics and Growth Mechanism Study. *ACS Nano* **2015**, 9, 6119–6127.

39. Jianyi Chen , Bo Liu , Yanpeng Liu , Wei Tang , Chang Tai Nai , Linjun Li , Jian Zheng, Libo Gao, Yi Zheng, Hyun Suk Shin, Hu Young Jeong, and Kian Ping Loh Chemical Vapor Deposition of Large-Sized Hexagonal WSe2 Crystals on Dielectric Substrates. *Adv. Mater.* **2015**, 27, 6722–6727.

40. Cheng, R.; Li, D.; Zhou, H.; Wang, C.; Yin, A.; Jiang, S.; Liu, Y.; Chen, Y.; Huang, Y.; and Duan, X. Electroluminescence and Photocurrent Generation from Atomically Sharp WSe2/MoS2 Heterojunction p−n Diodes. *Nano Lett.* **2014**, 14, 5590−5597.

41. Wang, Tianjiao; Andrews, Kraig; Bowman, Arthur; Hong, Tu; Koehler, Michael; Yan, Jiaqiang; Mandrus, David,; Zhou, Zhixian; and Xu, Ya-Qiong High-Performance WSe2 Phototransistors with 2D/2D Ohmic Contacts. *Nano Lett.* **2018**, 18, 2766−2771.

42. Yin, Chong; Wng, Xudong; Chen, Yan; Li, Dan; Lin, Tie; Sun, Shuo; Shen, Hong; Du, Piyi; Sun, Sun, Jinglan; Meng, Xiangjian; Chu, Junhao; Wong, Hon Fai; Leung, Chi Wah; Wang, Zongrong; and Wang, Jianlu A Ferroelectric Relaxor Polymer-Enhanced P-Type WSe2 Transistor. *Nanoscale* **2018**, 10, 1727-1734.

43. Benjamin, Christopher J.; Zhanga, Suki; and Chen, Zhihong Controlled Doping of Transition Metal Dichalcogenides by Metal Work Function Tuning in Phthalocyanine Compounds. *Nanoscale*, **2018**, 10, 5148-5153.

44. Jin, Youngjo; Keum, Dong Hoon; An, Sung-Jin; Lim, Joonggyu; Lee, Hyun Seok; Lee, Young Hee; Van Der Waals, A. Homojunction: Ideal p–n Diode Behavior in MoSe2. *Adv. Mat.* **2015**, 27, 5534-5540.

45. Suh, Joonki; Park, Tae-Eon; Lin, Der-Yuh; Fu, Deyi; Park, Joonsuk; Jung, Hee Joon; Chen, Yabin; Ko, Changhyun; Jang, Chaun; Sun, Yinghui; Sinclair, Robert; Chang, Joonyeon

Tongay, Sefaattin; and Wu, Junqiao Doping against the Native Propensity of MoS2: Degenerate Hole Doping by Cation Substitution, *Nano Lett.* **2014**, 14 (12), 6976–6982.

46. Zhao, Peida; Kiriya , Daisuke; Azcatl, Angelica; Zhang, Chenxi; Tosun, Mahmut; Liu, Yi-Sheng; Hettick, Mark; Kang, Jeong Seuk; McDonnell, Stephen; KC, Santosh, Guo, Jinghua; Cho, Kyeongjae, Wallace, Robert M.; and Javey, Ali Air Stable p-Doping of WSe2 by Covalent Functionalization. *ACS Nano* **2014**, 8 (10), pp 10808–10814.

47. Chen, Mikai; Nam, Hongsuk; Wi, Sungjin; Ji, Lian; Ren, Xin; Bian, Lifeng; Lu, Shulong; and Liang, Xiaogan Stable Few-Layer MoS2 Rectifying Diodes Formed by Plasma-Assisted Doping. *Appl. Phys. Lett.* **2013**, 103, 142110.

48. Nipane, Ankur; Karmakar, Debjani; Kaushik, Naveen; Karande, Shruti; and Lodha, Saurabh Few-Layer MoS2 p-Type Devices Enabled by Selective Doping Using Low Energy Phosphorus Implantation. *ACS Nano* **2016**, 10, 2128–2137.

49. Chen, Chang-Hsiao; Wu, Chun-Lan; Pu, Jiang; Chiu, Ming-Hui; Kumar, Pushpendra Kum; Takenobu, Taishi, and Li, Lain-Jong Hole Mobility Enhancement and P -Doping in Monolayer WSe2 by Gold Decoration. *2D Mater.* **2014**, 1, 034001.

50. Fang, H.; Tosun, M.; Seol, G.; Chang, T. C.; Takei, K.; Guo, J.; Javey, A. Degenerate n-Doping of Few-Layer Transition Metal Dichalcogenides by Potassium. *Nano Lett.* **2013**, 13 (5), 1991−1995.

51. Du, Y.; Liu, H.; Neal, A. T.; Si, M.; Ye, P. D. Molecular Doping of Multilayer MoS2 Field-Effect Transistors: Reduction in Sheet and Contact Resistances. *IEEE Electron Device Lett.* **2013**, 34, 1328−1330.

52. Kiriya, D.; Tosun, M.; Zhao, P.; Kang, J. S.; Javey, A. Air-Stable Surface Charge Transfer Doping of MoS2 by Benzyl Viologen. *J. Am. Chem. Soc.* **2014**, 136, 7853−7856.

53. Duan, X.; Wang, C.; Fan, Z.; Hao, G.; Kou, L.; Halim, U.; Li, H.; Wu, X.; Wang, Y.; Jiang, J.; Pan, A.; Huang, Y.; Yu, R.; Duan, X. Synthesis of WS2xSe2–2x Alloy Nanosheets with Composition-Tunable Electronic Properties. *Nano Lett.* **2016**, 16, 264-269.

54. Ye, J. T.; Zhang, Y. J.; Akashi, R.; Bahramy, M. S.; Arita, R.; Iwasa, Y. Superconducting Dome in a Gate-Tuned Band Insulator. *Science* **2012**, 338, 1193.

55. Suh, J.; Park, T.-E.; Lin, D.-Y.; Fu, D.; Park, J.; Jung, H. J.; Chen, Y.; Ko, C.; Jang, C.; Sun, Y.; Sinclair, R.; Chang, J.; Tongay, S.; Wu, Junqiao Doping against the Native Propensity of MoS2: Degenerate Hole Doping by Cation Substitution. *J. Nano Lett.* **2014**, 14 (12), 6976−6982.

56. Gao, Jian; Kim, Young Duck; Liang, Liangbo; Idrobo, Juan Carlos; Chow, Phil; Tan, Jiawei; Li, Baichang; Li, Lu; Sumpter, Bobby G.; Lu, Toh-Ming, Meunier, Vincent; Hone, James; Koratkar, Nikhil Transition-Metal Substitution Doping in Synthetic Atomically Thin Semiconductors. *Adv. Mat.* **2016**, 28, 9735-9743.

57. Kang, Won Tae; Lee, Min; Yun, Seok Joon; Song, Young Il; Kim, Kunnyun; Kim, Do-Hwan; Shin, Yong Seon; Lee, Kiyoung; Heo, Jinseong; Kim, Young-Min; Lee, Young Hee; and Yu, Woo Jong Direct Growth of Doping Controlled Monolayer WSe2 by Selenium-Phosphorus Substitution. *Nanoscale* **2018**, Advance Article.

58. Fu, Yajun; Long, Mingsheng; Gao, Anyuan; Wang, Yu; Pan, Chen; Liu, Xiaowei; Zeng, Junwen; Xu, Kang; Zhang, Lili; Liu, Erfu; Hu, Weida; Wang, Xiaomu; and Miao, Feng; Intrinsic P-Type W-Based Transition Metal Dichalcogenide by Substitutional Ta-Doping, *Appl. Phys. Lett.* **2017**, 111, 043502.

59. Yang, L.; Majumdar, K.; Liu, H.; Du, Y.; Wu, H.; Hatzistergos, M.; Hung, P. Y.; Tieckelmann, R.; Tsai, W.; Hobbs, C.; Ye, P. D. High Performance Multilayer MoS2 Transistors with Scandium Contacts. *Nano Lett.* **2014**, 14 (11), 6275−6280.

60. Huang, C.; Wu, S.; Sanchez, A. M.; Peters, J. J. P.; Beanland, R.; Ross, J. S.; Rivera, P.; Yao, W.; Cobden, D. H.; Xu X. Intimate Contacts. *Nat. Mater.* **2014**, *13*, 1096.

61. Wang, S.; Rong, Y.; Fan, Y.; Pacios, M.; Bhaskaran, H.; He, K.; Warner, J. H. Shape Evolution of Monolayer MoS2 Crystals Grown by Chemical Vapor Deposition. *Chem. Mater.* **2014**, 26, 6371–6379.

62. Huang, J. K.; Pu, J.; Hsu, C. L.; Chiu, M. H.; Juang, Z. Y.; Chang, Y. H.; Chang, W. H.; Iwasa, Y.; Takenobu, T.; Li, L. J. Large-Area Synthesis of Highly Crystalline WSe2 Monolayers and Device Applications. *ACS Nano* **2014**, *8*, 923 .

63. Zhou, H.; Wang, C.; Shaw, J. C.; Cheng, R.; Chen, Y.; Huang, X.; Liu, Y.; Weiss, N. O.; Lin, Z.; Huang, Y.; Duan, X. Large Area Growth and Electrical Properties of P-Type WSe2 Atomic Layers. *Nano Lett.* **2015**, *15*, 709.

64. Wu, S.; Huang, C.; Aivazian, G.; Ross, J. S.; Cobden, D. H.; Xu, X. Vapor–Solid Growth of High Optical Quality MoS2 Monolayers with Near-Unity Valley Polarization. *ACS Nano* **2013**, *7*, 2768-2772.

65. Huang, C.; Wu, S.; Sanchez, A. M.; Peters, J. J. P.; Beanland, R.; Ross, J. S.; Rivera, P.; Yao, W.; Cobden, D. H.; Xu, X. Lateral Heterojunctions Within Monolayer MoSe2–WSe2 Semiconductors. *Nat. Mater.* **2014**, *13*, 1096-1101.

66. Wulff, G. *Z. Kristallogr.* **1901**, *34*, 449-530.

67. Lauritsen, J. V.; Bollinger, M. V.; Lægsgaard, E.; Jacobsen, K. W.; Nørskov, J. K.; Clausen, B. S.; Topsøe, H.; Besenbacher, F. Morphology and Atomic-Scale Structure of MoS2 Nanoclusters Synthesized with Different Sulfiding Agents. *J. Catal.* **2004**, *221*, 510-522.

68. Lee, Y. H.; Zhang, X. Q.; Zhang, W. J.; Chang, M. T.; Lin, C. T.; Chang, K. D.; Yu, Y. C.; Wang, J. T. W.; Chang, C. S.; Li, L. J.; *et al.* Synthesis of Large-Area MoS2 Atomic Layers with Chemical Vapor Deposition. *Adv. Mater.* **2012**, 24, 2320–2325.

69. Salitra, G.; Hodes, G.; Klein, E.; Tenne, R. Highly Oriented WSe2 Thin Films Prepared by Selenization of Evaporated WO3. *Thin Solid Films* **1994**, 245, 180–185.

70. Youichi Ohno, Electronic Structure of the Misfit-Layer Compounds PbTiS3 and SnNbS3. *Phys. Rev. B* **1991**, 44, 1281.

71. Li, H.; Lu, G.; Wang, Y.; Yin, Z.; Cong, C.; He, Q.; Wang, L.; Ding, F.; Yu, T.; Zhang, H. Mechanical Exfoliation and Characterization of Single- and Few-Layer Nanosheets of WSe2, TaS2, and TaSe2. *Small* **2013**, *9*, 1974.

72. W. Zhao , Z. Ghorannevis , A. K. Kumar , J. R. Pang , M. Toh , X. Zhang , C. Kloc , P. H. Tan , G. Eda Lattice dynamics in mono- and few-layer sheets of WS2 and WSe2. *Nanoscale* **2013**, *5*, 9677-9681.

73. Tonndorf, P.; Schmidt, R.; Böttger, P.; Zhang, X.; Börner, J.; Liebig, A.; Albrecht, M.; Kloc, C.; Gordan, O.; Zahn, D. R. T.; de Vasconcellos, S. M.; Bratschitsch, R. Photoluminescence Emission and Raman Response of Monolayer MoS2, MoSe2, and WSe2. *Opt. Express* **2013**, *21*, 4908-4916.

74. Duan, X.; Wang, C.; Shaw, J. C.; Cheng, R.; Chen, Y.; Li, H.; Wu, X.; Tang, Y.; Zhang, Q.; Pan, A.; Jiang, J.; Yu, R.; Huang, Y.; Duan, X. Lateral Epitaxial Growth of Two-

Dimensional Layered Semiconductor Heterojunctions. *Nat. Nanotechnol.* **2014**, *9*, 1024-1030.

75. Chuang, H.-J.; Tan, X.; Ghimire, N. J.; Perera, M. M.; Chamlagain, B.; Cheng, M. M.-C.; Yan, J.; Mandrus, D.; Tomanek, D.; Zhou, Z. High Mobility WSe2 p- and n-Type Field-Effect Transistors Contacted by Highly Doped Graphene for Low-Resistance Contacts. *Nano Lett.* **2014**, 14, 3594-3601.

76. Roy, T.; Tosun, M.; Kang, J. S.; Sachid, A. B.; Desai, S. B.; Hettick, M.; Hu, C. C.; Javey, A. Field-Effect Transistors Built from All Two-Dimensional Material Components. *ACS Nano* **2014**, 8, 6259-6264.

77. Kappera, R.; Voiry, D.; Yalcin, S. E.; Branch, B.; Gupta, G.; Mohite, A. D.; Chhowalla, M. Phase-engineered Low-Resistance Contacts for Ultrathin MoS2 transistors. *Nat. Mater.* **2014**, 13, 1128-1134.

78. Leong, W. S.; Luo, X.; Li, Y.; Khoo, K. H.; Quek, S. Y.; Thong, J. T. L. Low Resistance Metal Contacts to MoS2 Devices with Nickel-Etched-Graphene Electrodes. *ACS Nano* **2015**, 9, 869-877.

79. Onofrio, N.; Guzman, D.; and Strachan, A. Novel Doping Alternatives for Single-Layer Transition Metal Dichalcogenides. *J. Appl. Phys*. **2017**, 122, 185102.

80. Kresse, G. and Furthmüller, J., Efficient iterative schemes for ab initio total-energy calculations using a plane-wave basis set. *Physical review B* **1996,** 54, 11169.

81. Perdew, J.P., Burke, K. and Ernzerhof, M., Generalized gradient approximation made simple. *Physical Review Letters* **1996**, 77, 3865.

82. Blöchl, P.E., Projector augmented-wave method. *Physical Review B* **1994**, 50, 17953.

83. Momma, K. and Izumi, F., VESTA 3 for three-dimensional visualization of crystal, volumetric and morphology data. *Journal of applied crystallography* **2011**, 44, 1272.

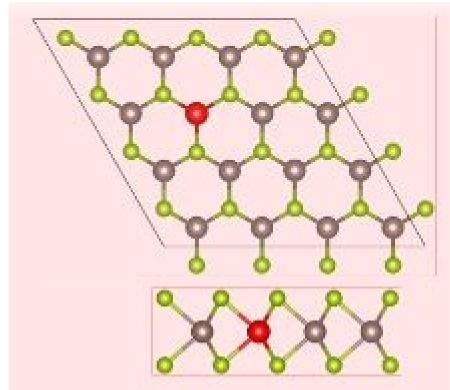

59x51mm (96 x 96 DPI)